Engineering 8 (2022) 170–180

Contents lists available at ScienceDirect

Engineering

journal homepage: www.elsevier.com/locate/eng

Research
Solid-State Batteries—Article

Modification of NASICON Electrolyte and Its Application in Real Na-Ion Cells

Qiangqiang Zhang [a,b,#], Quan Zhou [a,b,e,#], Yaxiang Lu [a,f,*], Yuanjun Shao [a,b], Yuruo Qi [a,b], Xingguo Qi [e], Guiming Zhong [c], Yong Yang [d], Liquan Chen [a,b], Yong-Sheng Hu [a,b,e,*]

[a] Key Laboratory for Renewable Energy, Beijing Key Laboratory for New Energy Materials and Devices, Beijing National Laboratory for Condensed Matter Physics, Institute of Physics, Chinese Academy of Sciences, Beijing 100190, China
[b] Center of Materials Science and Optoelectronics Engineering, University of Chinese Academy of Sciences, Beijing 100049, China
[c] Xiamen Institute of Rare-Earth Materials, Haixi Institutes, Chinese Academy of Sciences, Xiamen 361021, China
[d] State Key Laboratory of Physical Chemistry of Solid Surfaces & Department of Chemistry, College of Chemistry and Chemical Engineering, Xiamen University, Xiamen 361005, China
[e] HiNa Battery Technology Co., Ltd., Liyang 213300, China
[f] Yangtze River Delta Physics Research Center Co., Ltd., Liyang 213300, China

ARTICLE INFO

Article history:
Received 6 May 2020
Revised 24 August 2020
Accepted 14 September 2020
Available online 24 August 2021

Keywords:
Solid-state electrolytes
Solid-state sodium batteries
NASICON
Interface
Separator
Coating

ABSTRACT

The low ionic conductivity of solid-state electrolytes (SSEs) and the inferior interfacial reliability between SSEs and solid-state electrodes are two urgent challenges hindering the application of solid-state sodium batteries (SSSBs). Herein, sodium (Na) super ionic conductor (NASICON)-type SSEs with a nominal composition of $Na_{3+2x}Zr_{2-x}Mg_xSi_2PO_{12}$ were synthesized using a facile two-step solid-state method, among which $Na_{3.3}Zr_{1.85}Mg_{0.15}Si_2PO_{12}$ ($x = 0.15$, NZSP-$Mg_{0.15}$) showed the highest ionic conductivity of 3.54 mS·cm^{-1} at 25 °C. By means of a thorough investigation, it was verified that the composition of the grain boundary plays a crucial role in determining the total ionic conductivity of NASICON. Furthermore, due to a lack of examination in the literature regarding whether NASICON can provide enough anodic electrochemical stability to enable high-voltage SSSBs, we first adopted a high-voltage $Na_3(VOPO_4)_2F$ (NVOPF) cathode to verify its compatibility with the optimized NZSP-$Mg_{0.15}$ SSE. By comparing the electrochemical performance of cells with different configurations (low-voltage cathode vs high-voltage cathode, liquid electrolytes vs SSEs), along with an X-ray photoelectron spectroscopy evaluation of the after-cycled NZSP-$Mg_{0.15}$, it was demonstrated that the NASICON SSEs are not stable enough under high voltage, suggesting the importance of investigating the interface between the NASICON SSEs and high-voltage cathodes. Furthermore, by coating NZSP-$Mg_{0.15}$ NASICON powder onto a polyethylene (PE) separator (PE@NASICON), a 2.42 A·h non-aqueous Na-ion cell of carbon|PE@NASICON|$NaNi_{2/9}Cu_{1/9}Fe_{1/3}Mn_{1/3}O_2$ was found to deliver an excellent cycling performance with an 88% capacity retention after 2000 cycles, thereby demonstrating the high reliability of SSEs with NASICON-coated separator.

1. Introduction

Abundant and low-cost sodium (Na) resources provide a compelling reason to promote Na-ion batteries (NIBs) as promising candidates for large-scale energy-storage systems [1–9]. Solid-state sodium batteries (SSSBs) based on solid-state electrolytes (SSEs) have attracted great interest due to the higher degree of safety without using flammable liquid electrolytes (LEs) [10–13]. However, two main challenges still remain to be solved before the practical application of SSSBs: the low ionic conductivity of SSEs and the inferior interfacial reliability between SSEs and solid-state electrodes [10,11,14–18].

In 1976, Goodenough et al. [19] and Hong [20] conducted a pioneering work on Na super ionic conductor (NASICON)-type Na^+ SSEs, $Na_{1+x}Zr_2P_{3-x}Si_xO_{12}$ ($0 < x < 3$), which exhibit a considerably high conductivity due to open three-dimensional (3D) channels for fast Na^+ transport. The rigid 3D covalent network of NASICON-type SSEs consists of corner-sharing PO_4 tetrahedrons,

* Corresponding authors.
E-mail addresses: yxlu@iphy.ac.cn (Y. Lu), yshu@iphy.ac.cn (Y.-S. Hu).
# These authors contributed equally to this work.

https://doi.org/10.1016/j.eng.2021.04.028

SiO_4 tetrahedrons, and ZrO_6 octahedrons; each octahedron is connected to six tetrahedrons, while each tetrahedron is connected to four octahedrons, and the Na^+ cations are located in the interstitial sites of the network structure. Furthermore, in the range of $1.8 \leq x \leq 2.2$, NASICONs show a monoclinic structure with a *C*2/*c* space group, while having a rhombohedral structure with an *R*3*c* space group at the remaining values of *x* [19,20]. In particular, monoclinic $Na_3Zr_2Si_2PO_{12}$, as the most promising NASICON-type SSE, exhibits the highest Na^+ conductivity of 0.67 mS·cm^{-1} at room temperature [10,14,17,21,22]. To further improve the ionic conductivity of NASICON-type SSEs, in addition to the traditional solid-state method [23], various sintering techniques such as a solution-assisted solid-state reaction [24], spark plasma sintering [25], the sol–gel route [26], and an additive-assisted solid-state process [27] have been employed, all of which significantly enhance the ionic conductivity. Even so, the solid-state method is still the most facile process. Aside from optimizing the synthesis process, doping the extrinsic elements is a remarkably efficient approach. Zhang et al. [26] developed a self-forming composite NASICON electrolyte by introducing La^{3+} with a nominal composition of $Na_{3.3}Zr_{1.7}La_{0.3}Si_2PO_{12}$, and thereby delivering a remarkably enhanced Na^+ conductivity of 3.4 mS·cm^{-1} at 25 °C. However, lanthanum (La) is an expensive rare earth element, which would considerably increase the cost of SSSBs [28,29]. Accordingly, there is an urgent need to develop SSSBs that can reach a high level of ionic conductivity using earth-abundant and cost-effective elements.

Although the ionic conductivity of NASICON is still lower than that of an organic LE, the magnitude of 1 mS·cm^{-1} is high enough to afford the stable operation of SSSBs at room temperature. Accordingly, the question of how to improve the reliability of the interface between SSEs and solid-state electrodes has become increasingly important [30]. Several interfacial engineering methods have been developed for alleviating the impedance between sodium metal and NASICON, such as adding LE [31,32], inserting an *in situ* chemically formed interphase [33], sandwiching a polymer electrolyte [33], using a composite anode [34], using a 3D Na metal anode [35], chemically plating a layer [35–37], and using higher uniaxial compression [38]. Furthermore, various interfacial optimization processes have been proposed in order to reduce the resistance between the cathodes and NASICON, including co-sintering [39,40], adding an LE [28,31,32,35,36,41], introducing a plastic-crystal electrolyte [42], adding an ionic liquid [23,26], inserting a solid-state polymer electrolyte [33], mixing with a solid-state polymer electrolyte [35,43], using thin-film cathodes [44,45], and using 3D cathodes [24]. All of the SSSBs mentioned above adopted low average-voltage cathodes such as $Na_3V_2(PO_4)_3$ [23,24,26,35,36,39–42], sulfur (S) [31,32], $NaTi_2(PO_4)_3$ [33], $Na_2MnFe(CN)_6$ [43], $Na_{0.9}Cu_{0.22}Fe_{0.3}Mn_{0.48}O_2$ [28], or Na_xCoO_2 [44,45], although almost all of the values reported for the anodic electrochemical stabilities exceed 5 V [28,31,33,35,41]. It is worth noting that low average-voltage cathodes are unable to demonstrate the advantage of the high voltage of SSSBs or verify the feasibility of high-voltage NASICON-based SSSBs. Therefore, it is necessary to evaluate the sustainability of NASICON at a high potential by employing a high-voltage cathode.

Transition metal (TM)-based layer oxides are some of the most investigated cathodes in NIBs; however, numerous issues still exist and restrict the further improvement of NIB performance. One such problem is the dissolution of TM elements such as manganese (Mn), which would damage the crystal structure and induce the capacity fade, due to the decrease of valence-variable TM elements [46]. Furthermore, the dissolved TM cations may migrate and deposit onto the anode, thereby deteriorating the composition of the solid electrolyte interphase (SEI) and resulting in an unfavorable performance of the NIBs [47]. The use of a functional polymer separator with a coating layer is considered to be an effective strategy to suppress TM dissolution. Recently, Yan et al. [48] coated a compact NASICON-type $Li_{1.5}Al_{0.5}Ti_{1.5}(PO_4)_3$ (LATP) SSE layer onto a polyethylene (PE) separator, which efficiently inhibited TM dissolution from the $LiCoO_2$ and $LiMn_2O_4$ cathodes, as well as deposition on the anode electrode. In addition, coating an SSE layer onto a polypropylene (PP) and/or PE separator can remarkably enhances the wettability of the separator toward the LE and thus decrease the internal resistance of a battery, which facilitates the capacity release and enhances the battery's rate capability [49].

In this work, magnesium (Mg), an earth-abundant and cost-effective element, is introduced into NASICON by means of a facile solid-state method, resulting in significantly enhanced ionic conductivity, mainly contributed from the grain boundary. With the optimal nominal composition of $Na_{3.3}Zr_{1.85}Mg_{0.15}Si_2PO_{12}$ (NZSP-$Mg_{0.15}$), a high conductivity of 3.54 mS·cm^{-1} is achieved at 25 °C; to the best of our knowledge, this is the highest value that has been achieved among Mg-doped NASICON electrolytes. Based on the NZSP-$Mg_{0.15}$, SSSBs were constructed by employing a high-voltage $Na_3(VOPO_4)_2F$ (NVOPF) cathode and a metallic Na anode. To improve the electrode/electrolyte interfacial compatibility, around 5 μL·cm^{-2} of LE was added at the cathode side and carbon nanotubes (CNTs) were integrated with the Na metal anode. By comparing the electrochemical performance of the NVOPF|LE|NZSP-$Mg_{0.15}$|Na SSSBs cell with those of the NVOPF|LE|Na cell and the $Na_3V_2(PO_4)_3$ (NVP)|LE|NZSP-$Mg_{0.15}$|Na cell, it was found that the cathode-side interface was not stable enough. Furthermore, the results from the X-ray photoelectron spectroscopy (XPS) analysis of the after-cycled NZSP-$Mg_{0.15}$ pellets suggested a rise in the valence state of the NZSP-$Mg_{0.15}$. Our study therefore reveals the importance of studying the interface between NASICON SSEs and high-voltage cathodes in the future.

Moreover, kilogram-scale NZSP-$Mg_{0.15}$ NASICON powders were prepared and coated onto PE separators (PE@NASICON) after particle refinement, and a 2.42 A·h non-aqueous Na-ion cell of carbon|PE@NASICON|$NaNi_{2/9}Cu_{1/9}Fe_{1/3}Mn_{1/3}O_2$ using the coated PE separator was found to deliver an excellent cycling performance of 88% capacity retention after 2000 cycles at 1C rate, thereby demonstrating the high reliability and stability of a separator coated with NASICON-type SSEs.

2. Materials and methods

2.1. Materials

The reagents, which included sodium carbonate (Na_2CO_3, 99.95%, Acros Organics, USA), zirconium dioxide (ZrO_2, 99.99%, Shanghai Aladdin Bio-Chem Technology Co., Ltd., China (hereinafter referred to as Aladdin)), silicon dioxide (SiO_2, 99.9%, Alfa Aesar, USA (hereinafter referred to as Alfa)), ammonium phosphate monobasic ($NH_4H_2PO_4$, 99%, Aladdin), magnesium oxide (MgO, 99%, Alfa), vanadyl sulfate hydrate ($VOSO_4{\cdot}xH_2O$, 99.9%, Alfa), sodium phosphate monobasic dihydrate ($NaH_2PO_4{\cdot}2H_2O$, 99%, Sigma-Aldrich, USA), sodium fluoride (NaF, 99.99%, Aladdin), vanadium(III) oxide (V_2O_3, 99.7%, Alfa), sucrose (Alfa), hard carbon (HiNa Battery Technology Co., Ltd., China), and $NaNi_{2/9}Cu_{1/9}Fe_{1/3}Mn_{1/3}O_2$ (NNCFM, HiNa Battery Technology Co., Ltd., China), were used as received with no further treatment.

2.2. Preparation of NASICON ceramic pellets

Nominal composition of $Na_{3+2x}Zr_{2-x}Mg_xSi_2PO_{12}$ (x = 0, 0.05, 0.10, 0.15, 0.20) was synthesized and sintered into ceramic pellets using a traditional two-step solid-state method, as previously reported [23]. In a typical synthesis, under a stoichiometric ratio, Na_2CO_3, ZrO_2, SiO_2, $NH_4H_2PO_4$, and MgO were ball-milled in a planetary ball

mill (PM 400, Retsch GmbH, Germany) at 400 r·min^{-1} for 12 h. The as-prepared mixture was sintered at 1000 °C for 10 h in air. The as-sintered product was further ball-milled under the same conditions as mentioned above. The obtained powders were pressed into pellets with 15 mm in diameter; this was followed by a final sintering process at 1200 °C for 20 h, when the pellets were covered with mother powder.

2.3. Synthesis of NVOPF and NVP@C

NVOPF was synthesized using a facile low-temperature hydrothermal strategy, as previously reported [50]. In brief, all raw materials containing $VOSO_4{\cdot}xH_2O$, $NaH_2PO_4{\cdot}2H_2O$, and NaF were dissolved in deionized water to form a homogeneous solution, where the total molar ratio of V:P:F was 1:3:1.7. The homogeneous solution was then transferred to a polytetrafluoroethylene (PTFE)-lined stainless steel autoclave and maintained at 120 °C for 10 h. After the reaction, the products were collected by centrifugation and washed adequately with distilled water, followed by drying at 120 °C for 10 h to obtain the final products. The as-synthesized NVOPF has a single phase (Appendex A Fig. S1(a)) with a nano-sized morphology (Appendex A Fig. S1(b)). In addition, the lattice finger of the (103) plane in the transmission electron microscopy (TEM) image (Appendex A Fig. S1(c)) and the binding energy of the vanadium (V) element in the XPS spectrum (Appendex A Fig. S1(d)) further prove the composition of the as-prepared NVOPF cathode. NVP was prepared via a one-step solid-state method, according to our previous report [51]. In brief, the precursors containing V_2O_3 (10 mmol), $NaH_2PO_4{\cdot}2H_2O$ (30 mmol), and sucrose (1 g) were ball-milled in a planetary ball mill (PM 400) at 400 r·min^{-1} for 12 h, and then the mixture was sintered at 900 °C for 24 h under argon (Ar). The X-ray powder diffraction (XRD) pattern and scanning electron microscopy (SEM) image of the synthesized NVP cathode are presented in Figs. S2(a) and (b) in Appendex A, showing a pure phase with a nano-sized morphology.

2.4. Material characterization

XRD was carried out on a D8 ADVANCE X-ray diffractometer (Bruker Corporation, Germany) using copper (Cu) K_α radiation (λ = 1.5405 Å). SEM images were obtained on a Hitachi S-4800 (Hitachi, Japan). TEM was conducted on a JEOL JEM-2100F (JEOL, Japan) microscope equipped with a Gatan spectrometer Gif Quantum 965 (Gatan Inc., USA). XPS was conducted using a Thermo Scientific ESCLAB 250Xi (Thermo Fisher Scientific, USA) equipped with monochromic aluminum (Al) K_α radiation, and all spectra were calibrated for the charging effect with the C 1s peak at 284.8 eV. Linear sweep voltammetry (LSV) was recorded on a CHI800D electrochemical workstation (Shanghai Chenhua Instrument Co., Ltd., China). Electrochemical impedance spectroscopy (EIS, ZAHNER-elektrik GmbH & Co. KG, Germany) was performed on a Solartron electrochemical workstation with a frequency range from 10 MHz to 1 Hz and an alternating current amplitude of 10 mV. Nuclear magnetic resonance (NMR) spectra were recorded on a 400 MHz AVANCE III HD spectrometer (Bruker Corporation, Germany). The chemical shift of ^{31}P was referenced to 1 mol·L^{-1} H_3PO_4 aqueous solution (0 part per million (ppm)), respectively. The ^{31}P magic-angle spinning (MAS) NMR spectra were obtained using a single pulse with a recycle delay of 60 and 90 s at a spinning frequency of 12 kHz.

2.5. Electrochemical measurements

All the galvanostatic measurements of the solid-state batteries assembled in Swagelok cells and the liquid-state batteries assembled in coin cells were conducted on a Land BT2000 battery test system (Wuhan LAND Electronic Co., Ltd., China). The NVOPF cathode sheets were prepared by mixing NVOPF, Super phosphorus (P), and PTFE in a mass ratio of 7:2:1, followed by rolling the composite into thin square slices that were subsequently dried at 120 °C under a high vacuum overnight. The active material loading was about 3 mg·cm^{-2}. The NVP cathode sheets were prepared by mixing NVP, Super P, and polyvinylidene fluoride (PVDF) at a weight ratio of 7:2:1 in an appropriate *N*-methyl pyrrolidone (NMP) solution to make a homogeneous slurry to spread on Al foil, which was subsequently dried at 120 °C under a high vacuum overnight. The active material loading was about 3 mg·cm^{-2}. The cut-off voltage was maintained between 2.8 and 4.3 V for the NVOPF cathode and between 2.7 and 3.7 V for the NVP. The anode was prepared by mixing sodium metal and CNT in a mass ratio of 90:10 under 300 °C, and then cooling it to room temperature for application. In particular, in order to assemble the solid-state batteries, sodium was attached on one side of the NASICON pellet and 5 μL·cm^{-2} of 1 mol·L^{-1} $NaClO_4$/PC and 5% (mass fraction) fluoroethylene carbonate (FEC) LE was added at the cathode side to improve wettability. All liquid-state coin cells used the same LE as mentioned above. All cells were assembled in a glove box under Ar. During the charge and discharge process, the same current rate was used. Furthermore, based on the PE@NASICON separator, 2.42 A·h 26650-type cylindrical Na-ion cells using hard carbon as the anode and NNCFM as the cathode were manufactured by HiNa Battery Technology Co., Ltd.

3. Results and discussion

Doping extrinsic elements in $Na_{1+x}Zr_2P_{3-x}Si_xO_{12}$ ($0 < x < 3$) is a remarkably efficient approach to improve the ionic conductivity; the elements that have been doped are summarized in Appendix A Table S1. However, it should be noted that most of the doped-NASICONs exhibited several impure phases in comparison with undoped-NASICON, probably due to the large difference in ionic radius and charge. Thus, the most likely case when doping NASICON is that extrinsic elements are precipitated in the grain boundary and the composition of the grain is modified; the composition of the grain boundary and grain are then adjusted simultaneously to achieve better performance.

Fig. 1(a) shows XRD patterns of the undoped and Mg-doped NASICON, labeled as NZSP-Mg_0, NZSP-$Mg_{0.05}$, NZSP-$Mg_{0.10}$, NZSP-$Mg_{0.15}$, and NZSP-$Mg_{0.20}$, respectively. All XRD results reveal the ZrO_2 impurity phase in agreement with previous reports, which is difficult to eliminate. The Mg-doped NASICON presents more ZrO_2 along with a new $NaMgPO_4$ impurity phase. It has been reported that Mg^{2+} cannot act as the framework ions in NASICON [52,53]. Accordingly, here Mg translates into $NaMgPO_4$ and is distributed in the grain boundary. Thus, the contents of the Na and P in the NASICON decrease, while the silicon (Si) content relatively increases. Meanwhile, ZrO_2 dissolves poorly in silicate-containing compounds [54], so the ZrO_2 impurity phase was found to increase due to the increase in Si content after doping Mg in NASICON. In addition, according to the relationship between Na content and the NASICON phase formation mentioned above, NZSP-$Mg_{0.15}$ and NZSP-$Mg_{0.20}$ should be rhombohedral *R*3*c* NASICON [19,20]. However, all of the as-synthesized materials exhibit a monoclinic *C*2/*c* crystal structure, which can be confirmed by the diffraction peaks located at around 19.2° and 27.5°, as shown in Figs. 1(b) and (c). The XRD results further confirm that the Mg element does not substitute for Zr, whereas $NaMgPO_4$ consumes Na in the nominal composition $Na_{3+2x}Zr_{2-x}Mg_xSi_2PO_{12}$ (x = 0, 0.05, 0.10, 0.15, 0.20). In brief, doping with Mg decorates the grain and the grain boundary of NASICON simultaneously.

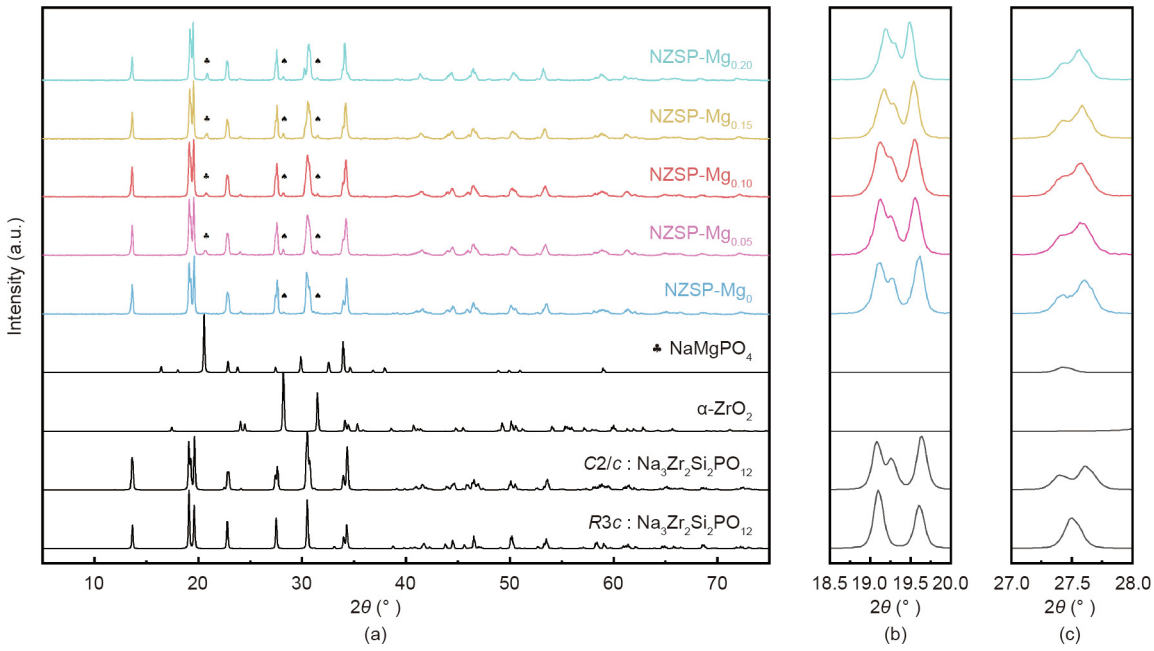

Fig. 1. (a) XRD patterns of the nominal composition $Na_{3+2x}Zr_{2-x}Mg_xSi_2PO_{12}$ (x = 0, 0.05, 0.10, 0.15, 0.20) samples corresponding to NZSP-Mg_0, NZSP-$Mg_{0.05}$, NZSP-$Mg_{0.10}$, NZSP-$Mg_{0.15}$, and NZSP-$Mg_{0.20}$, respectively. (b, c) Magnifications of the angles range from (b) 18.5° to 20.0° and (c) 27.0° to 28.0° from (a). 2θ: diffraction angle; a.u.: arbitrary unit.

To obtain more information about the structure and composition of the as-synthesized products, solid-state ^{31}P NMR spectra were acquired for quantitative analysis. In Fig. 2, an additional peak can be observed for Mg-doped NASICON, compared with undoped NASICON. The peak located at around −11 ppm can be recognized as the phosphate in NASICON, whereas the peak located at around 6 ppm is attributed to $NaMgPO_4$, as demonstrated in Fig. 1(a). Furthermore, with an increase of Mg content, the peak of NASICON gradually shifts to the lower field, corresponding to the increment of the Si/P ratio. In addition, the intensity of the peak located at around 6 ppm gradually increases with more Mg content, suggesting that the amount of $NaMgPO_4$ is increased.

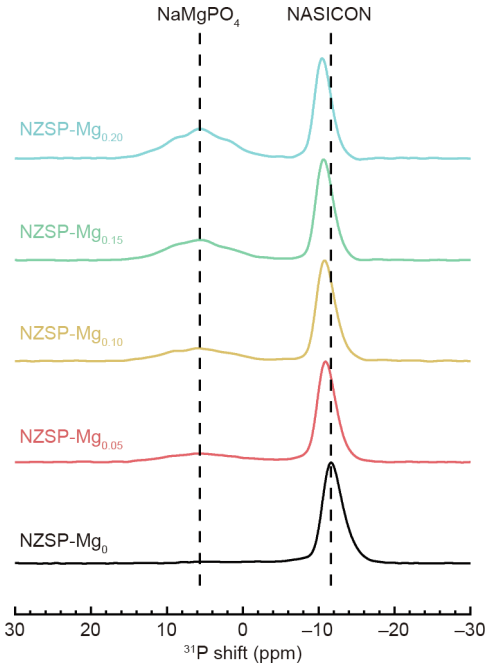

Fig. 2. Solid-state ^{31}P NMR spectra of NZSP-Mg_0, NZSP-$Mg_{0.05}$, NZSP-$Mg_{0.10}$, NZSP-$Mg_{0.15}$, and NZSP-$Mg_{0.20}$ samples.

In order to investigate the distribution of $NaMgPO_4$ more intuitively, transmission electron microscopy–electron energy loss spectroscopy (TEM–EELS) mapping was conducted, as shown in Fig. 3. It is noticeable that the Mg element is mainly distributed at the edge of the particles representing the grain boundary, while the P element is also distributed differently between the inner area and the outer edge, due to different concentrations of P in $NaMgPO_4$ and $Na_{3+2x}Zr_{2-x}Si_2PO_{12}$. These results further confirm the existence of $NaMgPO_4$ in the grain boundary, and are consistent with the conclusion obtained from XRD.

The microstructure of NASICON usually exerts a significant influence on the final ionic conductivity [23,55,56], and a larger grain size usually induces a higher ionic conductivity [57]. Fig. 4 presents an optical photograph (Fig. 4(a)) and SEM images (Figs. 4(b)–(f)) of the as-synthesized products. It can be seen that NZSP-$Mg_{0.05}$ exhibits a similar micromorphology to undoped NASICON due to the low Mg content, while a higher Mg content results in a larger grain size. Therefore, we expect that the ionic conductivity of NASICON can be improved by doping with Mg.

The resistances of the as-prepared nominal composition $Na_{3+2x}Zr_{2-x}Mg_xSi_2PO_{12}$ (x = 0, 0.05, 0.10, 0.15, 0.20) electrolytes were measured by EIS at temperatures ranging from −100 to 40 °C. The ionic conductivities were calculated according to the following equation [58,59]:

$$\sigma = \frac{l}{RS}$$

where σ is the ionic conductivity, l is the thickness of the ceramic pellet, R is the measured resistance, and S is the area of the ceramic pellet. Information on the sizes of the ceramic pellets is listed in Appendix A Table S2, and the resulting Arrhenius behaviors are summarized in Figs. 5(a)–(c). The activation energies were calculated via the Arrhenius equation [16,58,60]:

$$\sigma = \frac{A}{T} e^{-\frac{E_a}{k_B T}}$$

where A is the pre-exponential factor, T is the absolute temperature, E_a is the activation energy of diffusion, and k_B is the Boltzmann constant.

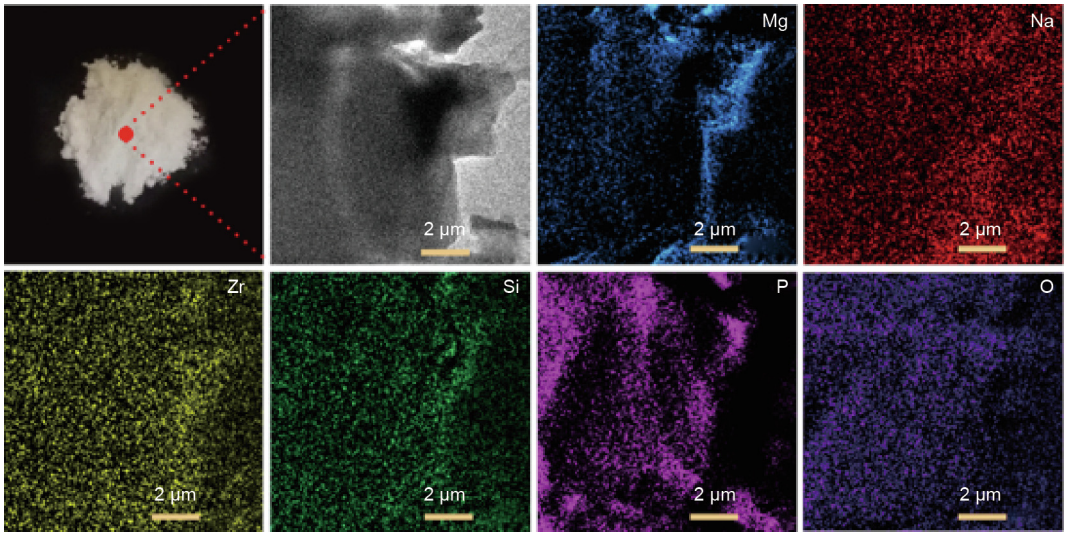

Fig. 3. TEM–EELS mapping of the NZSP-$Mg_{0.15}$ sample.

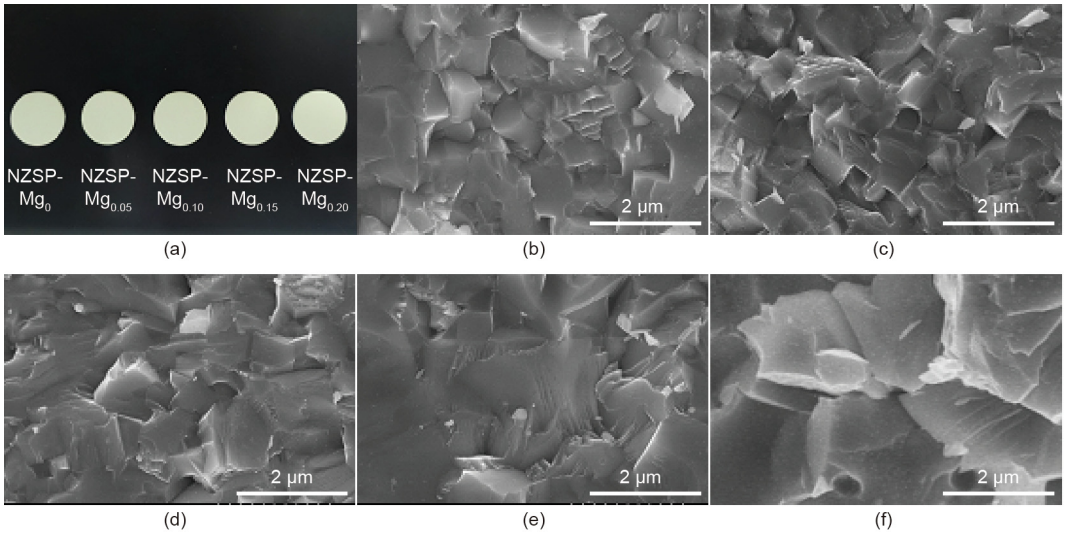

Fig. 4. (a) Optical photographs of NZSP-Mg_0, NZSP-$Mg_{0.05}$, NZSP-$Mg_{0.10}$, NZSP-$Mg_{0.15}$, and NZSP-$Mg_{0.20}$ samples. (b–f) SEM images of (b) NZSP-Mg_0, (c) NZSP-$Mg_{0.05}$, (d) NZSP-$Mg_{0.10}$, (e) NZSP-$Mg_{0.15}$, and (f) NZSP-$Mg_{0.20}$.

It can be seen from Fig. 5(a) that, with increasing amounts of Mg substitution, the total conductivity (σ_t) of NASICON also increases in the whole range of measured temperatures until reaching NZSP-$Mg_{0.15}$. In complex impedance spectra, it is difficult to distinguish the resistances from the grain and the grain boundary because the plots will merge at a high measuring temperature. Based on the equation $\omega_{max}RC = 1$ (where ω_{max} is the frequency of maximum loss in the impedance spectrum, R is the resistance of the constituent component, and C is the capacity of the constituent component, which is usually constant for a definite component) [61], it is necessary to decrease the measuring temperature to obtain a higher R value so that the impedances of the grain and grain boundary can be separated at the frequency range of the workstation, as exemplified by the impedance spectrum of NZSP-$Mg_{0.15}$ at −100 °C (Appendex A Fig. S3). Figs. 5(b) and (c) show the Arrhenius behaviors of the grain boundary and the grain, respectively, at temperatures from −100 to −10 °C. It can be seen that the σ of the grain boundary (σ_{gb}) changes more drastically than that of the grain (σ_g), and the σ_{gb} increases with the increment of Mg substitution until reaching NZSP-$Mg_{0.15}$. Given the XRD results, the enhancement of σ_{gb} is attributed to the generation of $NaMgPO_4$ (Mg-doped Na_3PO_4), which is an ionic conductor [29,60]. The effect of space charge contributes to fast ionic diffusion at the grain boundary as well [26]. Moreover, NZSP-$Mg_{0.20}$ exhibits a similar σ_{gb}, so the higher σ_t possessed by NZSP-$Mg_{0.15}$ in comparison with NZSP-$Mg_{0.20}$ is due to the higher σ_g, as evidenced in Fig. 5(c). This is because NZSP-$Mg_{0.20}$ consumes more Na to form $NaMgPO_4$, thereby decreasing the Na^+ concentration in the grain; therefore, NZSP-$Mg_{0.20}$ exhibits a lower σ_g and thus a lower σ_t in comparison with NZSP-$Mg_{0.15}$.

The densities of the as-synthesized products were measured and are presented in Table 1, showing that the density of NASICON decreases with increasing amounts of Mg substitution, which is believed to be adverse to the σ_t [57,62]. Therefore, the density results further confirm the crucial role of the grain boundary in increasing the ionic conductivity. Fig. 5(d) shows the impedance spectrum of NZSP-$Mg_{0.15}$ at 25 °C. This sample has the highest ionic conductivity (3.54 mS·cm^{-1} at 25 °C) among the as-prepared NASICON samples; this value is also the highest among the reported Mg-doped NASICON electrolytes. It should be noted that

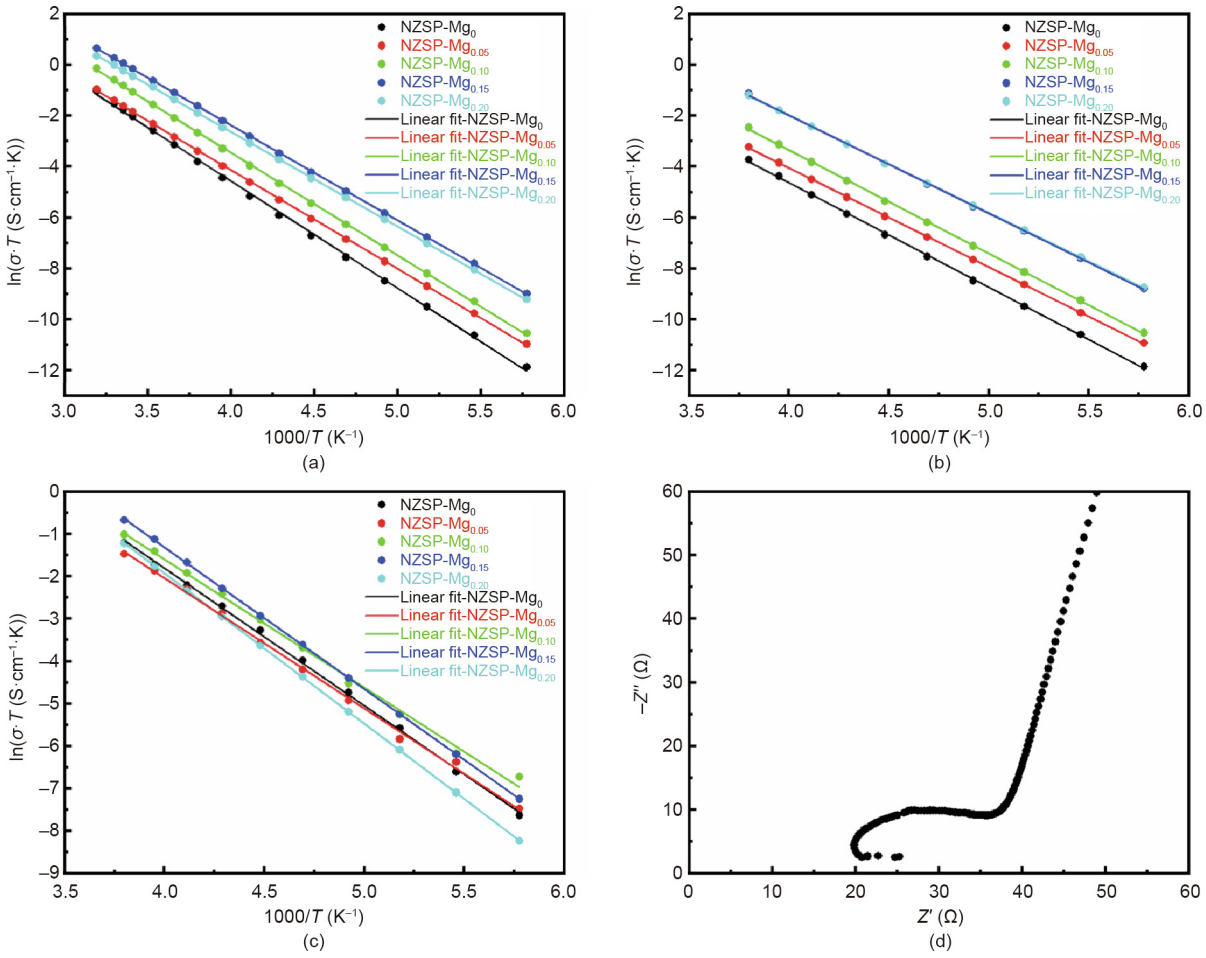

Fig. 5. Arrhenius plots of (a) total conductivity, (b) grain boundary conductivity, and (c) grain conductivity vs reciprocal temperature. (d) Complex impedance plane plot of the NZSP-$Mg_{0.15}$ sample at 25 °C.

Table 1
Densities of the NZSP-Mg_0, NZSP-$Mg_{0.05}$, NZSP-$Mg_{0.10}$, NZSP-$Mg_{0.15}$, and NZSP-$Mg_{0.20}$ samples.

Sample	Density (g·cm^{-3})
NZSP-Mg_0	3.27
NZSP-$Mg_{0.05}$	3.27
NZSP-$Mg_{0.10}$	3.23
NZSP-$Mg_{0.15}$	3.15
NZSP-$Mg_{0.20}$	3.11

a Mg-doped NASICON was previously claimed to have a high conductivity of 3.5 mS·cm^{-1} at room temperature [31], but a contemporaneous article proved that the reported value was incorrect [29].

The interfacial compatibility between NASICON and the electrodes plays a key role in determining the electrochemical performance of SSSBs. In particular, low interfacial resistance, a chemically stable interphase, and a wide electrochemical stability window ensure the stable cycling of SSSBs. It has been reported that there is a high interfacial resistance between sodium metal and NASICON, which induces an inferior electrochemical performance of SSSBs, especially at room temperature [33,35,36,38,39,63]. Herein, in order to alleviate the interfacial impedance of the NASICON/Na anode, we introduced 10% (mass fraction) CNT into the sodium metal to decrease the surface tension and increase the wettability. The impedance spectrum of the symmetric Na|NZSP-$Mg_{0.15}$|Na cell at room temperature exhibits a small resistance, as shown in Fig. 6(a), which is low enough to allow the room-temperature operation of SSSBs. Moreover, galvanostatic Na stripping/plating at a current density of 0.1 mA·cm^{-2} demonstrates high stability despite a minor increment in the voltage polarization due to the formation of a passivation layer, as shown in Fig. 6(b) [43,63], suggesting a high interfacial stability between sodium metal and NASICON. Galvanostatic Na stripping/plating at different current densities was also carried out, as shown in Appendix A Fig. S4, and the critical current density of 1 mA·cm^{-2} indicated high interfacial stability. In addition to cathodic stability, the anodic electrochemical stability of NASICON is crucial for SSSBs; high oxidation resistance would make it possible to use high-voltage cathodes for high energy density. Most reports claim that the anodic electrochemical stability of NASICON exceeds 5 V by using LSV or cyclic voltammetry (CV) tests [28,31,33,35,41]. In the present study, we also carried out LSV measurement of Au|NASICON|Na to determine the anodic stability (Fig. 6(c)). According to the LSV curve, the anodic electrochemical window is around 4.62 V if the value is based on the crossover point of two tangent lines, as is done in the literature, while the threshold value is 3.75 V if the oxidation current is taken as the starting point. Fig. 6(d) presents schematic illustrations of the Na|NZSP-$Mg_{0.15}$|Na cell and the Au|NZSP-$Mg_{0.15}$|Na cell.

Running a battery is a direct way to verify the feasibility of NASICON functioning under a high voltage. Sodium cathodes with an average voltage lower than 3.75 V have commonly been used in

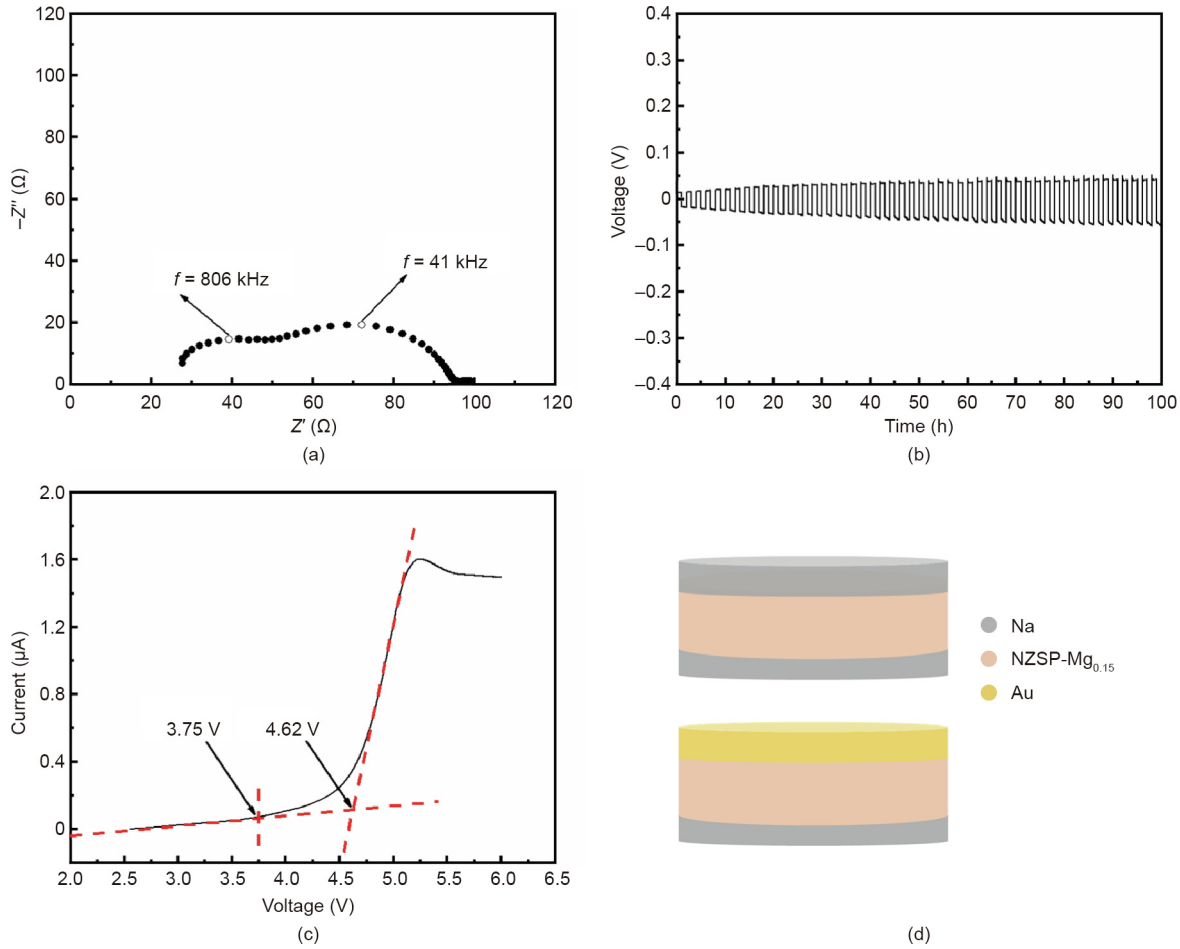

Fig. 6. (a) Complex impedance plane plot of the Na|NZSP-$Mg_{0.15}$|Na symmetric cell at 25 °C. (b) Galvanostatic Na stripping/plating cycling of a Na|NZSP-$Mg_{0.15}$|Na symmetric cell at a current density of 0.1 mA·cm^{-2} with a capacity of 0.1 mA·h·cm^{-2} at 25 °C. (c) LSV of NZSP-$Mg_{0.15}$ at a scan rate of 0.01 mV·s^{-1}. (d) Schematic illustration of the Na|NZSP-$Mg_{0.15}$|Na cell and the Au|NZSP-$Mg_{0.15}$|Na from top to bottom.

NASICON-based SSSBs, and the high stability of NASICON is confirmed in the reports [26,35,42]. Herein, for the first time, we constructed SSSBs by employing a high-voltage NVOPF cathode. The fabricated NVOPF|LE|NZSP-$Mg_{0.15}$|Na SSSB delivered an initial discharge capacity of 113.9 mA·h·g^{-1} with a retention of 90.5% after 100 cycles at 1C at room temperature, as shown in Fig. 7(a). In order to investigate the reason for the capacity decay of NVOPF|LE|NZSP-$Mg_{0.15}$|Na SSSB, a controlled cell NVOPF|LE|Na liquid-state battery was constructed and operated under the same conditions as NVOPF|LE|NZSP-$Mg_{0.15}$|Na SSSB. The controlled cell battery exhibited a high first discharge capacity of 114.9 mA·h·g^{-1} with a high retention of 98.6% after 100 cycles, as presented in Fig. 7(b). This result indicates the high reliability of NVOPF with LE, and shows that NVOPF and LE are not the key factors resulting in the capacity decay of NVOPF|LE|NZSP-$Mg_{0.15}$|Na SSSBs. NVP|LE|NZSP-$Mg_{0.15}$|Na SSSB was also prepared and, as expected, demonstrated a high stability with a capacity retention of 98.8% after 100 cycles under the same working conditions as NVOPF|LE|NZSP-$Mg_{0.15}$|Na SSSB due to the low average working voltage, as shown in Fig. 7(c).

Fig. S5 in Appendex A presents the first and 100th charge–discharge curve of the NVOPF|LE|NZSP-$Mg_{0.15}$|Na cell (Fig. S5(a)), the NVOPF|LE|Na cell (Fig. S5(b)), and the NVP|LE|NZSP-$Mg_{0.15}$|Na cell (Fig. S5(c)) at 1C. Fig. 7(d) presents schematic illustrations of the NVOPF|LE|NZSP-$Mg_{0.15}$|Na cell, the NVOPF|LE|Na cell, and the NVP|LE|NZSP-$Mg_{0.15}$|Na cell, respectively. Accordingly, we infer that NASICON may be unstable under high voltage. The evolution of NZSP-$Mg_{0.15}$ on the cathode-side surface of the NVOPF|LE|NZSP-$Mg_{0.15}$|Na SSSBs was probed by XPS before and after galvanostatic cycling tests, as shown in Fig. 8. The Zr 3d, Si 2p, P 2p, and Mg 1s peaks all shift toward higher binding energies, indicating that the NZSP-$Mg_{0.15}$ has been oxidized under high voltage during the electrochemical charge–discharge processes. The experimental results are in accordance with previous theoretical calculations, which revealed that the anodic electrochemical stability of NASICON was lower than 4 V [64,65]. Thus, the decomposition potential of NASICON should be recognized based on the starting point of the oxidation current rather than the crossover point of two tangent lines of the LSV or CV profiles.

Based on the highly conductive NZSP-$Mg_{0.15}$ SSE, a PE@NASICON separator was prepared. Fig. 9(a) provides an SEM image of the surface morphology of the PE@NASICON, which shows that the irregular NZSP-$Mg_{0.15}$ particles with a size distribution in the range of 500–1000 nm are uniformly coated on the surface of the PE separator. Based on the PE@NASICON separator, we then constructed 2.42 A·h 26650-type cylindrical Na-ion cells using hard carbon as the anode and NNCFM as the cathode; the average voltage of these cells is 3 V versus Na^+/Na. According to the results above, the PE@NASICON is electrochemically stable with an NNCFM cathode. The first formation cycle was carried out to construct a stable SEI on the electrode surfaces; the charge and discharge profile is presented in Fig. S6 in Appendex A. A discharge capacity of 2.74 A·h was obtained at 0.1C in the voltage range of 1.5–4.0 V. After the first formation cycle, the full cell was cycled

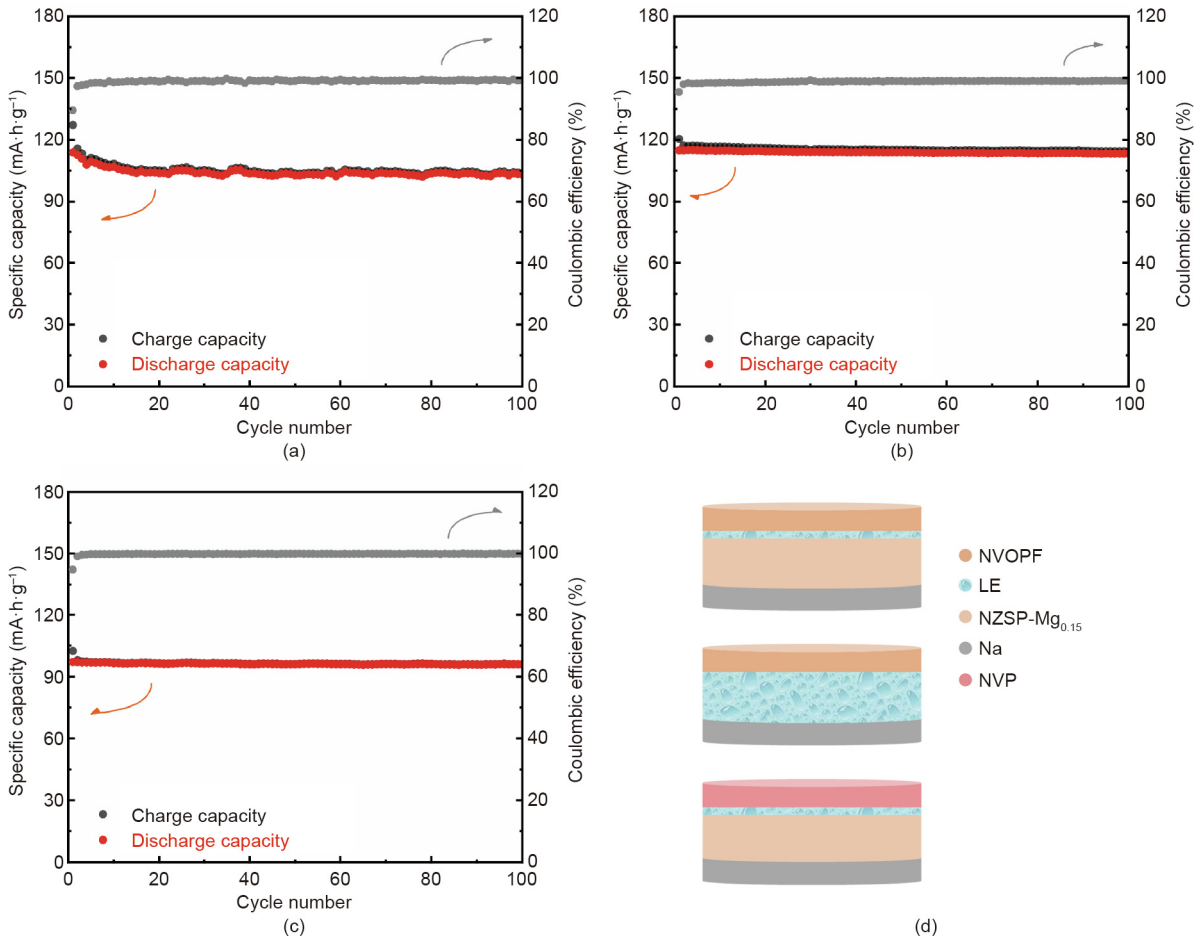

Fig. 7. Cycling performance of (a) the NVOPF|LE|NZSP-$Mg_{0.15}$|Na cell, (b) the NVOPF|LE|Na cell, and (c) the NVP|LE|NZSP-$Mg_{0.15}$|Na cell at room temperature. (d) Schematic illustration of the NVOPF|LE|NZSP-$Mg_{0.15}$|Na cell, the NVOPF|LE|Na cell, and the NVP|LE|NZSP-$Mg_{0.15}$|Na cell, respectively, from top to bottom.

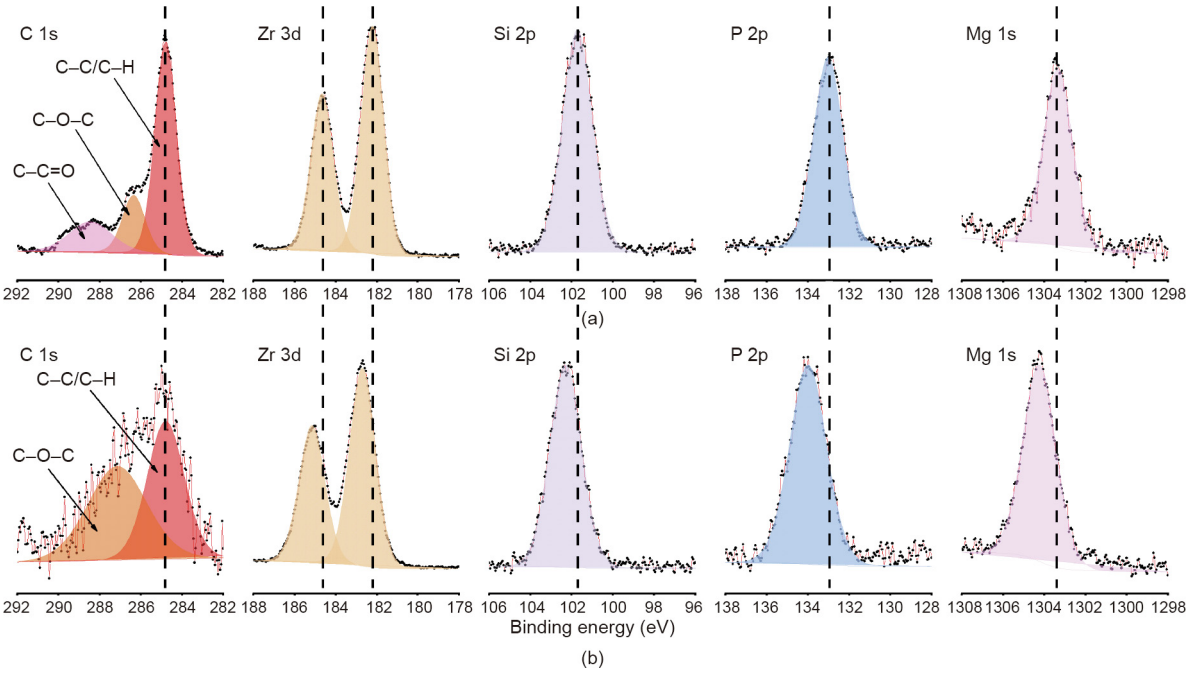

Fig. 8. Characterization of the surface of the NZSP-$Mg_{0.15}$ sample (a) before and (b) after the galvanostatic cycling test from the SSSBs. XPS spectra of C 1s, Zr 3d, Si 2p, P 2p, and Mg 1s.

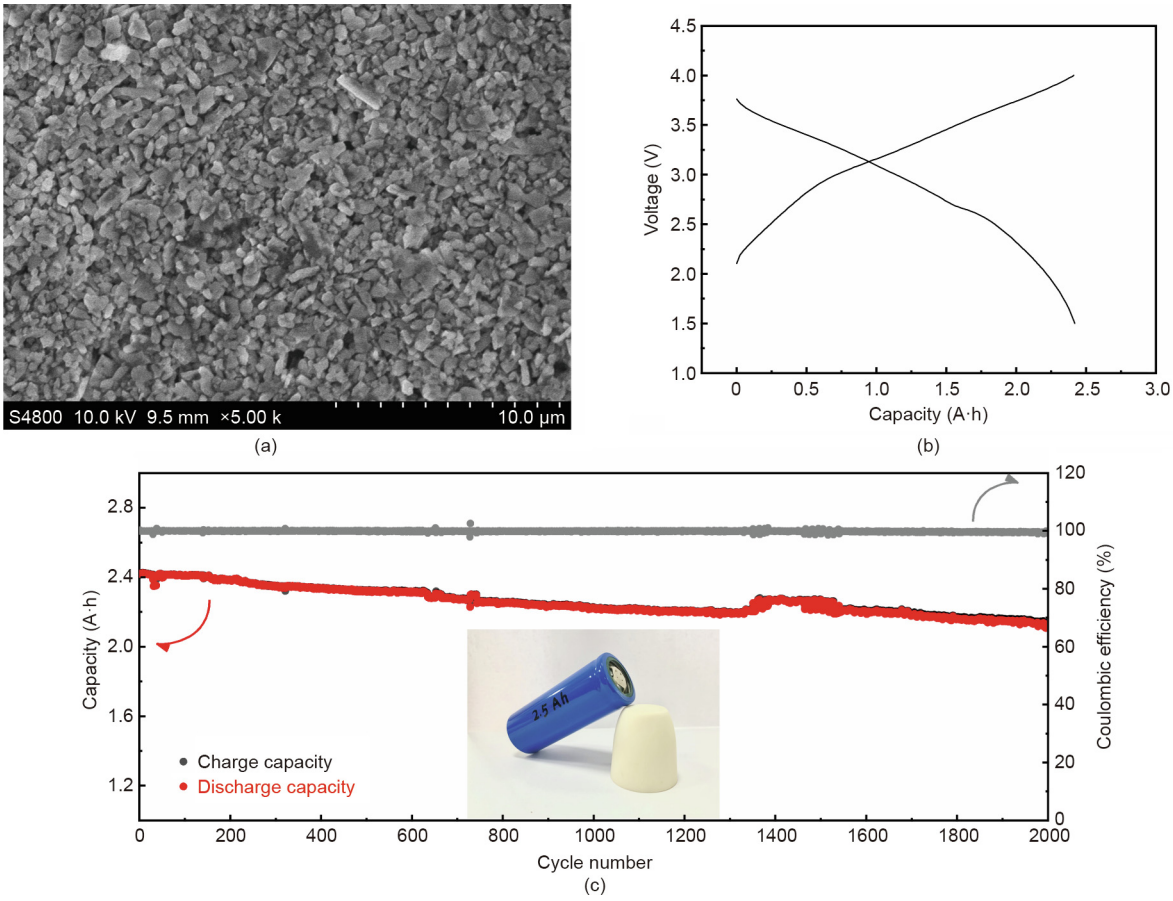

Fig. 9. (a) Surface morphologies of PE@NASICON; (b) charge–discharge curve of hard carbon|PE@NASICON|NNCFM at 1C; (c) cycling performance of hard carbon|PE@NASICON|NNCFM at 1C. Inset is a digital photo of the 2.42 A·h 26650-type cylindrical Na-ion cell.

under a 1C current rate, delivering a 2.42 A·h discharge capacity, as presented in Fig. 9(b). The full cell exhibits outstanding cycling performance, with 88% capacity retention after 2000 cycles, as shown in Fig. 9(c). The inset in Fig. 9(c) is a digital photo of the 2.42 A·h 26650-type cylindrical Na-ion cell. The remarkable performance benefits from the high reliability and stability of the PE@NASICON separator. NZSP-$Mg_{0.15}$ is compatible with the NNCFM cathode, and the functional coating layer can suppress TM dissolution and maintain the structural stability of the NNCFM cathode. Furthermore, coating an NZSP-$Mg_{0.15}$ SSE layer onto the PE separator remarkably enhances the wettability of the separator toward the LE and thus decreasing the internal resistance of the battery to achieve the outstanding performance of the full cell. Therefore, NASICON SSEs are a promising functional material for application in separator optimization.

4. Conclusions

In conclusion, a cost-efficient Mg-doped NASICON was synthesized using a facile solid-state method, and the highest conductivity of 3.54 mS·cm^{-1} at 25 °C was achieved among the reported Mg-doped NASICON electrolytes with the nominal composition of NZSP-$Mg_{0.15}$. By means of XRD, NMR, and TEM–EELS mapping, it was confirmed that the Mg element is not located in the crystal lattice of NASICON; instead, the Mg precipitates in the grain boundary in addition to forming $NaMgPO_4$ ionic conductor. This behavior of Mg simultaneously modifies the composition of the grain and the grain boundary, and thereby enhancing the ionic conductivity of the NASICON. Furthermore, based on the optimized NZSP-$Mg_{0.15}$, we were the first to adopt the high-voltage NVOPF as the cathode in order to verify the feasibility of high-voltage NASICON-based SSSBs. By comparing the electrochemical performance of the NVOPF|LE|NZSP-$Mg_{0.15}$|Na SSSBs cell with those of the NVOPF|LE|Na cell and the NVP|LE|NZSP-$Mg_{0.15}$|Na cell, the anodic electrochemical stability of NZSP-$Mg_{0.15}$ was evaluated, and was shown to be insufficiently stable. XPS examination of the after-cycled NZSP-$Mg_{0.15}$ pellets suggested a rise in the valence state of NZSP-$Mg_{0.15}$, further demonstrating the poor stability with high-voltage cathodes. Our study demonstrates that it is urgent to develop effective strategies to enable a stable interface between NASICON SSEs and high-voltage cathodes. In addition, based on a PE@NASICON separator, a 2.42 A·h 26650-type cylindrical full cell was built and exhibited a remarkable cycling performance with 88% capacity retention after 2000 cycles. This result suggests that NASICON SSEs are a promising functional material for application in separator modification.

Acknowledgments

This work was supported by the National Key Technologies Research and Development Program, China (2016YFB0901500), the Opening Project of the Key Laboratory of Optoelectronic Chemical Materials and Devices, Ministry of Education, Jianghan University (JDGD-201703), the National Natural Science Foundation of China (51725206 and 51421002), the Strategic Priority Research Program of the Chinese Academy of Sciences (XDA21070500), and the Youth Innovation Promotion Association, Chinese Academy of Sciences (2020006).

Compliance with ethics guidelines

Qiangqiang Zhang, Quan Zhou, Yaxiang Lu, Yuanjun Shao, Yuruo Qi, Xingguo Qi, Guiming Zhong, Yong Yang, Liquan Chen, and Yong-Sheng Hu declare that they have no conflict of interest or financial conflicts to disclose.

Appendix A. Supplementary data

Supplementary data to this article can be found online at https://doi.org/10.1016/j.eng.2021.04.028.

References

[1] Zhao S, Qin B, Chan KY, Li CY, Li F. Recent development of aprotic Na–O_2 batteries. Batter Supercaps 2019;2(9):725–42.
[2] Lang J, Li J, Zhang F, Ding X, Zapien JA, Tang Y. Sodium-ion hybrid battery combining an anion-intercalation cathode with an adsorption-type anode for enhanced rate and cycling performance. Batter Supercaps 2019;2(5):440–7.
[3] Zhao C, Lu Y, Chen L, Hu YS. Flexible Na batteries. InfoMat 2020;2(1):126–38.
[4] Lin Z, Xia Q, Wang W, Li W, Chou S. Recent research progresses in ether- and ester-based electrolytes for sodium-ion batteries. InfoMat 2019;1(3):376–89.
[5] Hu YS, Lu Y. 2019 Nobel Prize for the Li-ion batteries and new opportunities and challenges in Na-ion batteries. ACS Energy Lett 2019;4(11):2689–90.
[6] Li Y, Yang Y, Lu Y, Zhou Q, Qi X, Meng Q, et al. Ultralow-concentration electrolyte for Na-ion batteries. ACS Energy Lett 2020;5(4):1156–8.
[7] Eshetu GG, Elia GA, Armand M, Forsyth M, Komaba S, Rojo T, et al. Electrolytes and interphases in sodium-based rechargeable batteries: recent advances and perspectives. Adv Energy Mater 2020;10(20):2000093.
[8] Hu Pu, Wang X, Ma J, Zhang Z, He J, Wang X, et al. $NaV_3(PO_4)_3$/C nanocomposite as novel anode material for Na-ion batteries with high stability. Nano Energy 2016;26:382–91.
[9] Hu P, Wang X, Wang T, Chen L, Ma J, Kong Q, et al. Boron substituted $Na_3V_2(P_{1-x}B_xO_4)_3$ cathode materials with enhanced performance for sodium-ion batteries. Adv Sci 2016;3(12):1600112. Correction in: Adv Sci 2017;4(2).
[10] Wang Y, Song S, Xu C, Hu N, Molenda J, Lu Li. Development of solid-state electrolytes for sodium-ion battery—a short review. Nano Mater Sci 2019;1(2):91–100.
[11] Huang Y, Zhao L, Li L, Xie M, Wu F, Chen R. Electrolytes and electrolyte/electrode interfaces in sodium-ion batteries: from scientific research to practical application. Adv Mater 2019;31(21):1808393.
[12] Liu L, Qi X, Yin S, Zhang Q, Liu X, Suo L, et al. *In situ* formation of a stable interface in solid-state batteries. ACS Energy Lett 2019;4(7):1650–7.
[13] Qiao L, Judez X, Rojo T, Armand M, Zhang H. Review—polymer electrolytes for sodium batteries. J Electrochem Soc 2020;167(7):070534.
[14] Zhou C, Bag S, Thangadurai V. Engineering materials for progressive all-solid-state Na batteries. ACS Energy Lett 2018;3(9):2181–98.
[15] Zhao C, Liu L, Qi X, Lu Y, Wu F, Zhao J, et al. Solid-state sodium batteries. Adv Energy Mater 2018;8(17):1703012.
[16] Lu Y, Li L, Zhang Q, Niu Z, Chen J. Electrolyte and interface engineering for solid-state sodium batteries. Joule 2018;2(9):1747–70.
[17] Hou W, Guo X, Shen X, Amine K, Yu H, Lu J. Solid electrolytes and interfaces in all-solid-state sodium batteries: progress and perspective. Nano Energy 2018;52:279–91.
[18] Zhang XQ, Zhao CZ, Huang JQ, Zhang Q. Recent advances in energy chemical engineering of next-generation lithium batteries. Engineering 2018;4(6):831–47.
[19] Goodenough JB, Hong HYP, Kafalas JA. Fast Na^+-ion transport in skeleton structures. Mater Res Bull 1976;11(2):203–20.
[20] Hong HYP. Crystal structures and crystal chemistry in the system $Na_{1+x}Zr_2Si_xP_{3-x}O_{12}$. Mater Res Bull 1976;11(2):173–82.
[21] Zhang Z, Shao Y, Lotsch B, Hu YS, Li H, Janek J, et al. New horizons for inorganic solid state ion conductors. Energy Environ Sci 2018;11(8):1945–76.
[22] Jalalian-Khakshour A, Phillips CO, Jackson L, Dunlop TO, Margadonna S, Deganello D. Solid-state synthesis of NASICON ($Na_3Zr_2Si_2PO_{12}$) using nanoparticle precursors for optimisation of ionic conductivity. J Mater Sci 2020;55(6):2291–302.
[23] Shao Y, Zhong G, Lu Y, Liu L, Zhao C, Zhang Q, et al. A novel NASICON-based glass–ceramic composite electrolyte with enhanced Na-ion conductivity. Energy Storage Mater 2019;23:514–21.
[24] Lan T, Tsai CL, Tietz F, Wei XK, Heggen M, Dunin-Borkowski RE, et al. Room-temperature all-solid-state sodium batteries with robust ceramic interface between rigid electrolyte and electrode materials. Nano Energy 2019;65:104040.
[25] Lee JS, Chang CM, Lee YIL, Lee JH, Hong SH. Spark plasma sintering (SPS) of NASICON ceramics. J Am Ceram Soc 2004;87(2):305–7.
[26] Zhang Z, Zhang Q, Shi J, Chu YS, Yu X, Xu K, et al. A self-forming composite electrolyte for solid-state sodium battery with ultralong cycle life. Adv Energy Mater 2017;7(4):1601196.
[27] Noi K, Suzuki K, Tanibata N, Hayashi A, Tatsumisago M. Liquid-phase sintering of highly Na^+ ion conducting $Na_3Zr_2Si_2PO_{12}$ ceramics using Na_3BO_3 additive. J Am Ceram Soc 2018;101(3):1255–65.
[28] Yang J, Wan HL, Zhang ZH, Liu GZ, Xu XX, Hu YS, et al. NASICON-structured $Na_{3.1}Zr_{1.95}Mg_{0.05}Si_2PO_{12}$ solid electrolyte for solid-state sodium batteries. Rare Met 2018;37(6):480–7.
[29] Samiee M, Radhakrishnan B, Rice Z, Deng Z, Meng YS, Ong SP, et al. Divalent-doped $Na_3Zr_2Si_2PO_{12}$ natrium superionic conductor: improving the ionic conductivity via simultaneously optimizing the phase and chemistry of the primary and secondary phases. J Power Sources 2017;347:229–37.
[30] Hu YS. Batteries: getting solid. Nat Energy 2016;1(4):16042.
[31] Song S, Duong HM, Korsunsky AM, Hu N, Lu L. A Na^+ superionic conductor for room-temperature sodium batteries. Sci Rep 2016;6(1):32330.
[32] Yu X, Manthiram A. Sodium–sulfur batteries with a polymer-coated NASICON-type sodium-ion solid electrolyte. Matter 2019;1(2):439–51.
[33] Zhou W, Li Y, Xin S, Goodenough JB. Rechargeable sodium all-solid-state battery. ACS Cent Sci 2017;3(1):52–7.
[34] Fu H, Yin Q, Huang Y, Sun H, Chen Y, Zhang R, et al. Reducing interfacial resistance by Na–SiO_2 composite anode for NASICON-based solid-state sodium battery. ACS Mater Lett 2020;2(2):127–32.
[35] Lu Y, Alonso JA, Yi Q, Lu L, Wang ZL, Sun C. A high-performance monolithic solid-state sodium battery with Ca^{2+} doped $Na_3Zr_2Si_2PO_{12}$ electrolyte. Adv Energy Mater 2019;9(28):1901205.
[36] Matios E, Wang H, Wang C, Hu X, Lu X, Luo J, et al. Graphene regulated ceramic electrolyte for solid-state sodium metal battery with superior electrochemical stability. ACS Appl Mater Interfaces 2019;11(5):5064–72.
[37] Miao X, Di H, Ge X, Zhao D, Wang P, Wang R, et al. AlF_3-modified anode-electrolyte interface for effective Na dendrites restriction in NASICON-based solid-state electrolyte. Energy Storage Mater 2020;30:170–8.
[38] Uchida Y, Hasegawa G, Shima K, Inada M, Enomoto N, Akamatsu H, et al. Insights into sodium ion transfer at the Na/NASICON interface improved by uniaxial compression. ACS Appl Energy Mater 2019;2(4):2913–20.
[39] Noguchi Y, Kobayashi E, Plashnitsa LS, Okada S, Yamaki JI. Fabrication and performances of all solid-state symmetric sodium battery based on NASICON-related compounds. Electrochim Acta 2013;101:59–65.
[40] Lalère F, Leriche JB, Courty M, Boulineau S, Viallet V, Masquelier C, et al. An all-solid state NASICON sodium battery operating at 200 °C. J Power Sources 2014;247:975–80.
[41] Ruan Y, Guo F, Liu J, Song S, Jiang N, Cheng B. Optimization of $Na_3Zr_2Si_2PO_{12}$ ceramic electrolyte and interface for high performance solid-state sodium battery. Ceram Int 2019;45(2):1770–6.
[42] Gao H, Xue L, Xin S, Park K, Goodenough JB. A plastic-crystal electrolyte interphase for all-solid-state sodium batteries. Angew Chem Int Ed Engl 2017;56(20):5541–5.
[43] Gao H, Xin S, Xue L, Goodenough JB. Stabilizing a high-energy-density rechargeable sodium battery with a solid electrolyte. Chem 2018;4(4):833–44.
[44] Kehne P, Guhl C, Ma Q, Tietz F, Alff L, Hausbrand R, et al. Electrochemical performance of all-solid-state sodium-ion model cells with crystalline Na_xCoO_2 thin-film cathodes. J Electrochem Soc 2019;166(3):A5328–32.
[45] Kehne P, Guhl C, Ma Q, Tietz F, Alff L, Hausbrand R, et al. Sc-substituted Nasicon solid electrolyte for an all-solid-state Na_xCoO_2/Nasicon/Na sodium model battery with stable electrochemical performance. J Power Sources 2019;409:86–93.
[46] Zhan C, Wu T, Lu J, Amine K. Dissolution, migration, and deposition of transition metal ions in Li-ion batteries exemplified by Mn-based cathodes—a critical review. Energy Environ Sci 2018;11(2):243–57.
[47] Zhang Q, Gu QF, Li Y, Fan HN, Luo WB, Liu HK, et al. Surface stabilization of O3-type layered oxide cathode to protect the anode of sodium ion batteries for superior lifespan. iScience 2019;19:244–54.
[48] Yan Z, Pan H, Wang J, Chen R, Luo F, Yu X, et al. Suppressing transition metal dissolution and deposition in lithium-ion batteries using oxide solid electrolyte coated polymer separator. Chin Phys B 2020;29(8):088201.
[49] Qi XG, Zhou Q, Tang K, Hu YS, inventors; HiNa Battery Technology Co., Ltd., assignee. [Ceramic separator and sodium ion secondary battery for sodium ion battery and its application]. Chinese Patent CN109244314A. 2019 Jan 18. Chinese.
[50] Qi Y, Zhao J, Yang C, Liu H, Hu Y. Comprehensive studies on the hydrothermal strategy for the synthesis of $Na_3(VO_{1-x}PO_4)_2F_{1+2x}$ ($0 \leq x \leq 1$) and their Na-storage performance. Small Methods 2019;3(4):1800111.
[51] Zhang Q, Lu Y, Yu H, Yang G, Liu Q, Wang Z, et al. PEO-$NaPF_6$ blended polymer electrolyte for solid state sodium battery. J Electrochem Soc 2020;167(7):070523.
[52] Tsai CL, Hong HYP. Investigation of phases and stability of solid electrolytes in the NASICON system. Mater Res Bull 1983;18(11):1399–407.
[53] Takahashi T, Kuwabara K, Shibata M. Solid-state ionics—conductivities of Na^+ ion conductors based on NASICON. Solid State Ion 1980;1(3–4):163–75.
[54] Vonalpen U, Bell M, Hofer H. Compositional dependence of the electrochemical and structural parameters in the Nasicon system ($Na_{1+x}Si_xZr_2P_{3-x}O_{12}$). Solid State Ion 1981;3-4:215–8.
[55] Fuentes RO, Figueiredo FM, Marques FMB, Franco JI. Processing and electrical properties of NASICON prepared from yttria-doped zirconia precursors. J Eur Ceram Soc 2001;21(6):737–43.
[56] Fuentes R. Influence of microstructure on the electrical properties of NASICON materials. Solid State Ion 2001;140(1–2):173–9.

[57] Naqash S, Sebold D, Tietz F, Guillon O. Microstructure–conductivity relationship of $Na_3Zr_2(SiO_4)_2(PO_4)$ ceramics. J Am Ceram Soc 2019;102(3):1057–70.
[58] Guin M, Tietz F, Guillon O. New promising NASICON material as solid electrolyte for sodium-ion batteries: correlation between composition, crystal structure and ionic conductivity of $Na_{3+x}Sc_2Si_xP_{3-x}O_{12}$. Solid State Ion 2016;293:18–26.
[59] Deng Y, Eames C, Nguyen LHB, Pecher O, Griffith KJ, Courty M, et al. Crystal structures, local atomic environments, and ion diffusion mechanisms of scandium-substituted sodium superionic conductor (NASICON). Chem Mater 2018;30(8):2618–30.
[60] Ben Bechir M, Ben Rhaiem A. The sodium-ion battery: study of alternative current conduction mechanisms on the Na_3PO_4-based solid electrolyte. Physica E 2020;120:114032.
[61] Irvine JTS, Sinclair DC, West AR. Electroceramics: characterization by impedance spectroscopy. Adv Mater 1990;2(3):132–8.
[62] Kim JH, Oh TS, Lee MS, Park JG, Kim YH. Effects of Al_2O_3 addition on the sinterability and ionic conductivity of nasicon. J Mater Sci 1993;28(6):1573–7.
[63] Wang S, Xu H, Li W, Dolocan A, Manthiram A. Interfacial chemistry in solid-state batteries: formation of interphase and its consequences. J Am Chem Soc 2018;140(1):250–7.
[64] Tang H, Deng Z, Lin Z, Wang Z, Chu IH, Chen C, et al. Probing solid–solid interfacial reactions in all-solid-state sodium-ion batteries with first-principles calculations. Chem Mater 2018;30(1):163–73.
[65] Lacivita V, Wang Y, Bo SH, Ceder G. *Ab initio* investigation of the stability of electrolyte/electrode interfaces in all-solid-state Na batteries. J Mater Chem A Mater Energy Sustain 2019;7(14):8144–55.